*Article*

# Positive and Negative Performance Analysis of the Bi-Directional Full-Flow Pump with an "S" Shaped Airfoil

Haifeng Jiao [1] , Mengcheng Wang [2], Haiyu Liu [3] and Songshan Chen [2,*]

1. College of Hydraulic Science and Engineering, Yangzhou University, Yangzhou 225000, China
2. College of Electrical, Energy and Power Engineering, Yangzhou University, Yangzhou 225000, China
3. College of Electrical Engineering, Yancheng Institute of Technology, Yancheng 224000, China
* Correspondence: yzcss08@163.com; Tel.: +86-138-1580-8923

**Abstract:** In this study, model tests and numerical simulations are conducted to study the bi-directional full-flow pump (BFFP). Firstly, the head, efficiency and shaft power of the BFFP are significantly higher in the positive operating condition than in the negative operating condition. When the unit operates in the positive direction, the clearance reflux flow rate, the flow uniformity and velocity-weighted average angle of the impeller inlet, and the intensity of pressure pulsation are significantly greater than those during the negative operation. When the pump unit is operating at low flow rates, the clearance reflux produces a significant disturbance to the impeller inlet main flow. Two vortices appear in the near-wall area of the clearance outlet (i.e., impeller inlet), and the range of vortices is larger in the positive operation than in the negative operation. Secondly, at low-flow and design-flow conditions, the total entropy production of the pump unit in the positive direction is greater than that in the negative direction. When at small- and design-flow rates, the amplitude of pressure pulsation in the positive direction is smaller than that in the negative direction. This study will contribute to the research and development of a full-flow pump.

**Keywords:** bi-directional full-flow pump; S-shaped airfoil; pressure pulsation; unsteady; entropy production rate; model test

## 1. Introduction

Since the 20th century, pump units operating in one direction have been widely used in industry and agriculture. Some of these projects have separately arranged diversion units and drainage units to meet the needs of different periods. With the development of the economy and environment, some pump station can no longer meet the current demand. Therefore, many scholars have proposed the transformation of the traditional unidirectional operating pumping units into pumping units that can operate in both directions [1–3].

At present, many scholars have conducted a lot of research on the hydraulic characteristics of bi-directional pumps. Meng et al. [4,5] researched the hydraulic performance of a bi-directional axial-flow pump. The research showed that the performance of the bi-directional pump in a negative operating condition is significantly worse than that in a positive operating condition. Under a low-flow condition, the deformation of the impeller blades is greater in a negative operation than in a positive operation. Conventional bi-directional pump impellers are of unidirectional design and have relatively poor performances in negative operations. Therefore, some scholars have conducted a lot of research on the "S" airfoil-type [6–8]. It was found that the "S" airfoil-type with center-symmetric design can ensure the similar hydraulic performance in positive and negative operation. The bi-directional pump with an "S" airfoil-type does not need to reverse the impeller by 180° in the negative operation. Reverse operation can be achieved by directly rotating the motor in reverse, which greatly saves the operation and management costs of the pumping station. Meanwhile, Ma et al. [9] compared the bi-directional pump unit using an

S airfoil-type and an arc airfoil-type. It was found that the bi-directional pump with an "S" airfoil-type can take into account both positive and negative operation performances. The comprehensive hydraulic performance of the "S" airfoil-type pump is remarkably better than that of the arc airfoil-type pump.

Unlike the structure of the axial flow pump, the full-flow pump (FFP) integrates the motor with the outer edge of the impeller and does not need to be driven by a drive shaft. Its flow channel also does not need to be designed in a curved shape and has a simple structure, so it is widely used in areas such as low-head pump stations and circulating cooling pumps. Shi et al. [10–12] showed that the clearance reflux of FFP leads to a lower performance than axial pump. When at a small flow rate, the pressure pulsation (PP) of the FFP is smaller compared with the axial-flow pump. The BFFP in this paper combines the advantages of FFP and "S" airfoil-type, so it is meaningful to study it.

Currently, many scholars study the pump performance mainly by external characteristics, PP, entropy production (EP) and vortex. Song et al. [13] studied the PP caused by free surface vortex in pump stations by experiment and numerical simulation. It was found that a free surface vortex tends to trigger low-frequency PP and induce unit resonance. Jiao et al. [14] found that the installation of the inlet guide vane at the impeller inlet of a shaft tubular pump could induce low-frequency PP. Yang et al. [15] studied the PP characteristics in the axial-flow-pump skip-shaped channel by using numerical simulation. It was found that the further away from the impeller, the smaller the amplitude of the main frequency of the PP. Zheng et al. [16] found that in the interstitial region of centrifugal pumps, pressure fluctuations are still determined by the blade passing frequency. The PP at the impeller outlet is greater than at other locations. Pankaj P. Gohil et al. [17] found that low-frequency, high-amplitude PP dominates in the turbine tail pipe at lower loading conditions. Ahmed et al. [18] found that the pressure of the axial flow pump increased along the direction of the impeller inlet to the outlet. The highest pressure value was found in the impeller outlet region. Yang et al. [19,20] investigated the energy-loss characteristics of an axial flow pump. Research has shown that the pressure energy loss in the impeller is the largest. The area where the energy loss occurs is mainly concentrated at the inlet and outlet ends of the blade. Meng et al. [21] studied the energy loss of a bi-directional axial-flow-pump. Research has shown that the EP is mainly concentrated at the impeller, regardless of a positive or negative operation. Feng et al. [22] studied the power failure transition process of centrifugal pumps. The energy loss of the centrifugal pump was found to be mainly related to the flow separation, backflow and vortex inside the flow field during the whole accidental-power-failure runaway process.

From the above study, it can be found that the external characteristics of the pump in the two operating directions are bound to be different. The characteristics of PP, entropy production rate (EPR) and vortex also have different degrees of difference. Therefore, this paper focuses on the study of the BFFP through the above aspects. Due to the small size of the BFFP model, the rotor motor is difficult to machine. Therefore, this paper still uses the drive shaft to drive the impeller. This paper focuses on the study of BFFP by combining numerical simulation and model testing [23–26]. Firstly, the test bench is designed and the PP and external characteristics of the "S" type BFFP unit are tested. Then, unsteady numerical simulations of the unit are performed. Finally, the accuracy of calculation is verified by model test. The research in this paper can play a positive role in the development of the FFP.

## 2. Numerical Calculation

### 2.1. Computational Model and Grid

The calculation model of the BFFP unit consists of impeller, stator and rotor clearance (SRC), inlet guide vane (IGV), guide vane (GV), GV diffusion section, and inlet and outlet water channels. The SZM35 hydraulic model is used for the impeller and GV of the BFFP, and Figure 1 shows the two-dimensional parameter diagram of the SZM35 impeller model. The impeller hub diameter $D_1$ is 120 mm. The impeller shroud diameter $D$ is 300 mm. The

number of impeller, GV and IGV blades are four, six and five, respectively. The impeller speed $n$ is 1421 r/min. The thickness $d$ of the SRC is 1 mm. The design flow rate is $Q_d$ = 297.3 L/s. Figure 2 display 3D model of the impeller "SZM35" and its internal flow diagram.
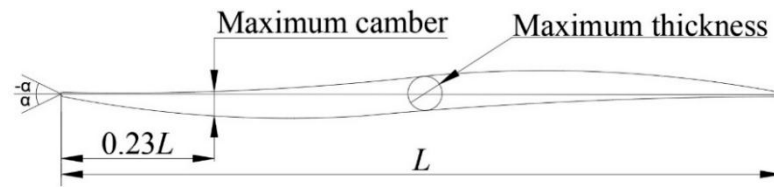


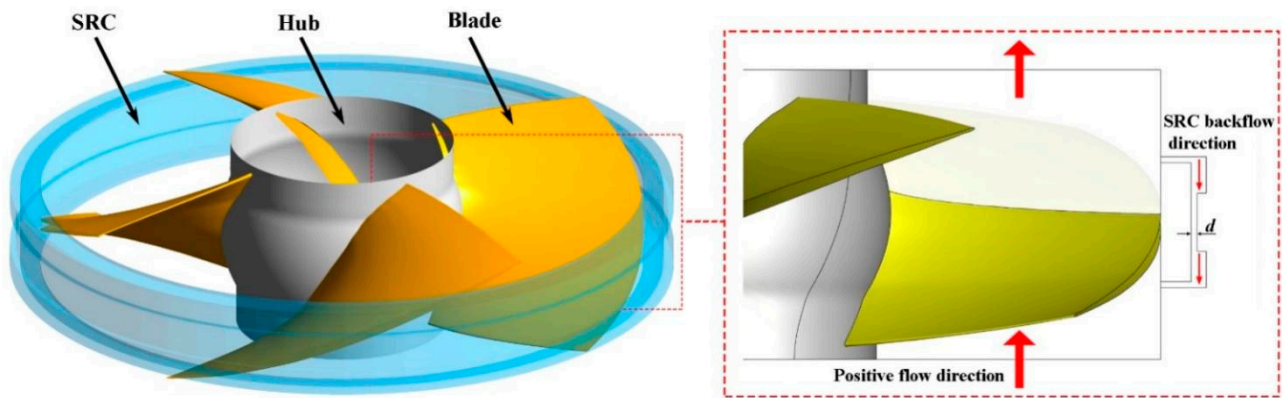**Figure 1.** Two-dimensional diagram of the "SZM35" hydrofoil.



**Figure 2.** A 3D model of the impeller "SZM35" and its internal flow diagram.

In order to increase the speed and accuracy of the calculations, structured grids were used for all parts of the pump unit. As the number of grids affects the convergence and accuracy of the simulation, a grid-independent analysis was performed for the BFFP model. The variations of the head with the number of grids are displayed in Figure 3. Figure 3 shows that once the number of grids reaches 6.17 million, increasing the number of grids has little effect on the head. Therefore, taking into account the calculation time, the total number of grids was determined to be 6.91 million. The grid information for each part of the pump unit is shown in Table 1. A computational model of the pump unit and the grids of each part are shown in Figure 4. The detailed grids of the SRC and impeller are shown in Figures 5 and 6.
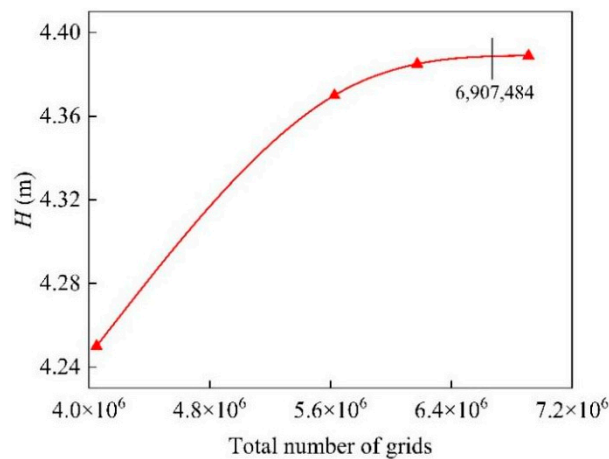


**Figure 3.** Grid-independent analysis.

**Table 1.** Grid information for each part of the computational model.

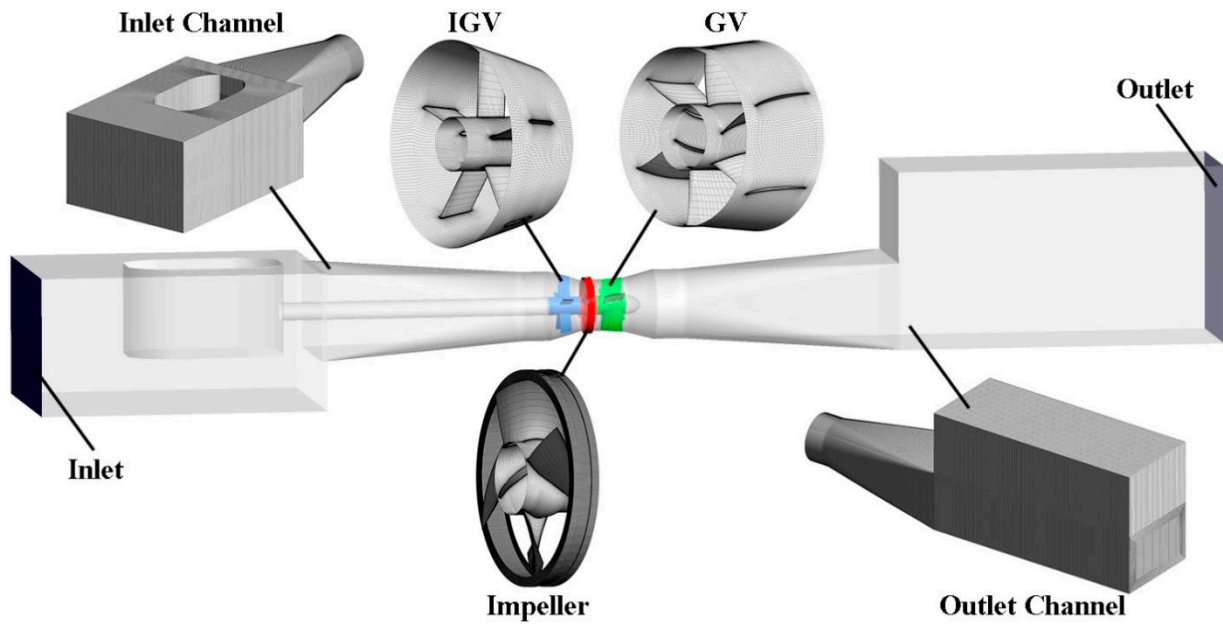| Part | Impeller | GV | IGV | Inlet Channel | Outlet Channel | SRC | GV Diffuser |
|---|---|---|---|---|---|---|---|
| Number of grids ($10^4$) | 66 | 81 | 65 | 226 | 136 | 77 | 40 |



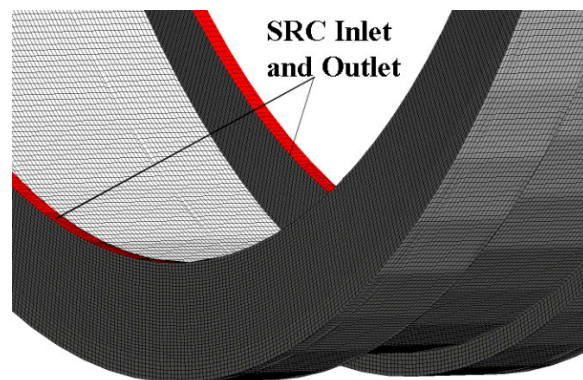**Figure 4.** Computational model of pump unit and grids of each part.



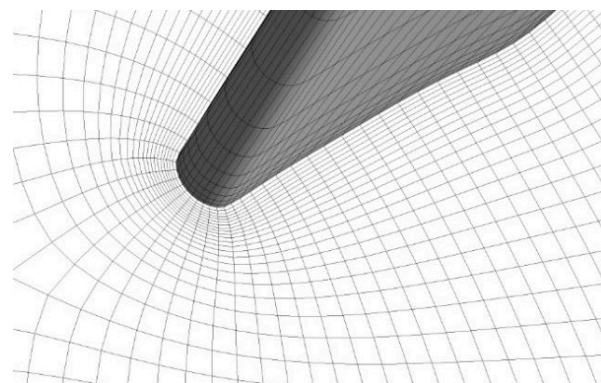**Figure 5.** Details of the SRC.



**Figure 6.** Details of the Impeller.

### 2.2. Control Equations

The N-S equation is chosen as the basic control equation for the calculations in this paper. Compared with the standard *k-ε* model, the RNG *k-ε* model adds terms to the *k* and *ε* transport equations and has a higher accuracy for high-speed flow and eddy flow. Since the flow at the clearance of the BFFP is complex, the RNG *k-ε* turbulence model is suitable for the numerical calculation. Although the flow at the clearance of the FFP is complex, the RNG *k-ε* turbulence model was found to be suitable for the numerical simulation of the FFP according to Shi et al. [27,28].

The *k* and *ε* equations in the RNG *k-ε* model are, respectively

$$\frac{\partial(\rho k)}{\partial(t)} + \frac{\partial(\rho k u_i)}{\partial(x_i)} = \frac{\partial}{\partial x_j}\left[\alpha_k \mu_{eff} \frac{\partial_k}{\partial x_j}\right] + \mu_t \left(\frac{\partial u_i}{\partial x_j} + \frac{\partial u_j}{\partial x_i}\right)\frac{\partial u_i}{\partial x_j} - \rho\varepsilon \tag{1}$$

$$\frac{\partial(\rho\varepsilon)}{\partial(t)} + \frac{\partial(\rho\varepsilon u_i)}{\partial(x_i)} = \frac{\partial}{\partial x_j}\left[\alpha_\varepsilon \mu_{eff} \frac{\partial_\varepsilon}{\partial x_j}\right] + \frac{C_{1\varepsilon} \bullet \varepsilon}{k}\mu_t \left(\frac{\partial u_i}{\partial x_j} + \frac{\partial u_j}{\partial x_i}\right)\frac{\partial u_i}{\partial x_j} - C_{2\varepsilon}\rho\frac{\varepsilon^2}{k} - R \tag{2}$$

where $x_i$ and $x_j$ represent the coordinate components; $\alpha_k$ and $\alpha_\varepsilon$ represent the corresponding coefficients of *k* and *ε*, respectively; $\rho$ means the fluid density; $\mu_{eff}$ represents the effective turbulent flow viscosity coefficient; $\mu_t$ represents the turbulent viscosity; $u_i$ and $u_j$ represent the time-averaged velocity components; $\mu_{eff} = \mu + \mu_t$; $\mu_t = \rho C_\mu \frac{k^2}{\varepsilon}$; $R = \frac{C_\mu \rho \varphi^3\left(1-\frac{\varphi}{\varphi_0}\right)\varepsilon^2}{(1+\beta\varphi^3)k}$; $C_\mu = 0.0845$; $C_{1\varepsilon} = 1.42$; $C_{2\varepsilon} = 1.68$; $\varphi = (2E_{ij})\frac{k}{\varepsilon}$; $E_{ij} = \frac{1}{2}\left(\frac{\partial u_i}{\partial x_j} + \frac{\partial u_j}{\partial x_i}\right)$; $\varphi_0 = 4.377$; and $\beta = 0.012$.

The momentum equation and the continuity equation are

$$\frac{\partial}{\partial t}(\rho u_i) + \frac{\partial}{\partial x_i}(\rho u_i u_j) = -\frac{\partial p}{\partial x_j} + \frac{\partial}{\partial x_j}\left(\mu\frac{\partial u_i}{\partial x_i} - \rho\overline{u_i' u_j'}\right) + S_i \tag{3}$$

$$\frac{\partial\rho}{\partial t} + \frac{\partial}{\partial x_i}(\rho u_i) = 0 \tag{4}$$

where *t* is the physical time; *p* is the local pressure; and $S_i$ is the Reynolds stress.

### 2.3. Boundary Conditions and Calculation Settings

First, the computational model in this paper was drawn using Unigraphics NX 12.0 software. Then, numerical simulations were performed using ANSYS CFX 2019 R3 software. Finally, post-processing was performed using CFD POST as well as TECPLOT. The inlet of the BFFP is set as a mass-flow inlet. The outlet is set as a static pressure outlet with a pressure value of 1 atm. The impeller is set as the rotating domain, while other sections are set as the static domain. The solid-wall surfaces include the blade surface, hub surface, shroud surface, SRC surface, channel surface, etc., and the boundary adopts the no-slip condition to satisfy the viscous fluid. The IGV and impeller, impeller and GV, and SRC and impeller were dynamic and static interfaces, which were set by the "transient frozen rotor" [29–31]. The rest of the interfaces in the pump device were static and static interface, with no need to set additional. Before the IGV, there was a long section of straight tube to accommodate the drive shaft, which was set to a solid wall and the boundary was set to a no-slip condition.

The size of the time step had an impact on the computational accuracy, and a time-step independent analysis of the device was performed, as shown in Figure 7. The results in Figure 7 show that the calculation results become more accurate as the value of the time step decreases. However, the difference between the results for time steps of $2.3458 \times 10^{-4}$ s and $1.1729 \times 10^{-4}$ s is smaller. Finally, the time step of $2.3458 \times 10^{-4}$ s (i.e., the time used to rotate the impeller by two degrees) was chosen with reference to the study of Zhang

et al. [32], Mu et al. [33] and Jin et al. [34] and the limitation of computational resources. The total time $t$ is 0.5911 s, which is the time for 14 rotations of the impeller.
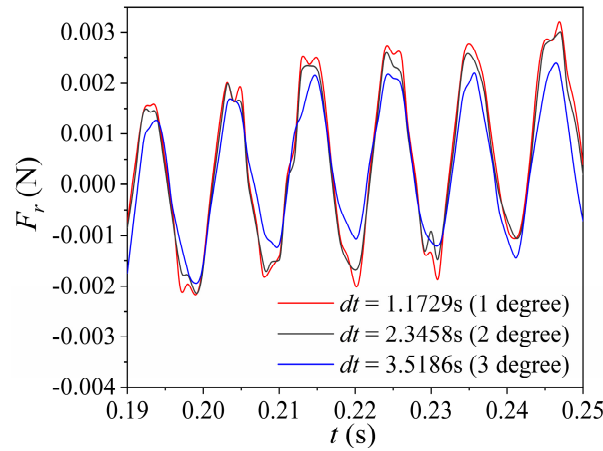


**Figure 7.** Time step independence analysis.

## 3. Results and Discussion

### 3.1. Analysis of Performance

Before the external characteristic analysis, the dimensionless parameters head coefficient $H_c$ and discharge coefficient $Q_c$ are introduced, and their respective equations are:

$$H_c = \frac{H}{H_d} \tag{5}$$

$$Q_c = \frac{Q}{Q_d} \tag{6}$$

where $H_d$ is the design head, m; $H$ is the head, m; $Q_d$ is the design flow rate, kg/s; $Q$ is the flow rate, kg/s.

In order to investigate the difference in performance of BFFP during the positive and negative operation, numerical simulations of the pump unit were performed. The head $H$, efficiency $\eta$ and shaft power $P$ of the pump unit were taken out for comparison, as shown in Figure 8. It can be found that when the flow rate increases, the efficiency first increases and then decreases, and the head and shaft power gradually decrease. The external characteristics of the BFFP have the same tendency in positive and negative operation. The head, efficiency and shaft power of the BFFP are significantly higher than those of the negative operation when it is running in the positive direction. The maximum efficiency of the unit is 59.74% in the positive operation and 52.89% in the negative operation. The difference in efficiency is about 6.85%. Under the design condition, the head difference in the two directions is about 1.46 m, and the efficiency difference is about 4.92%. Under the design condition, the shaft power difference is about 4.94 kW. Compared with the positive running condition, the performance curve of the unit shifted about 40 kg/s to the low flow rate in the negative running condition.
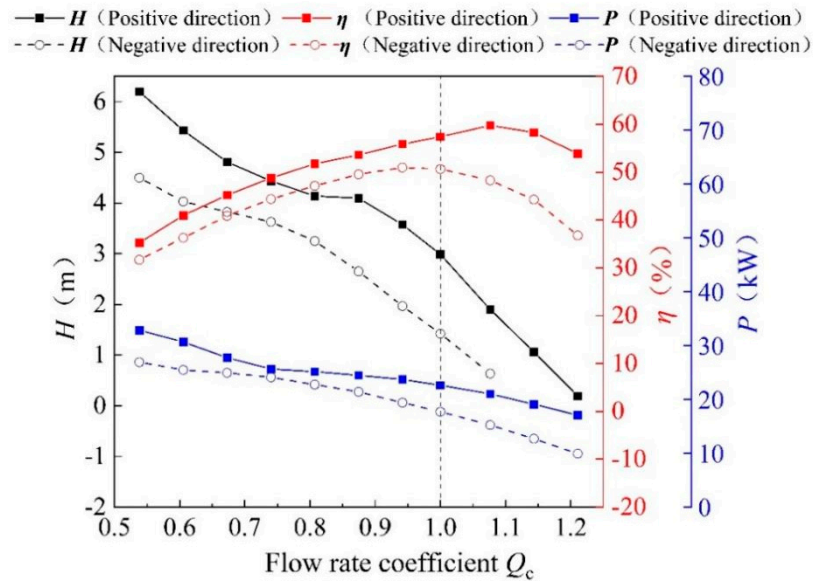
**Figure 8.** Head, efficiency and shaft power at each flow rate.

The difference in performance between the positive and negative operation of BFFP is obvious. The performance when running in the negative direction is significantly worse than the performance when running in the positive direction. In order to investigate the reason for the performance difference, the pressure difference (PD) $\Delta P$ between the inlet and outlet of the impeller, SRC reflux flow coefficient $Q_r$ of the BFFP are taken out for analysis. The results in Figure 9 show that the $Q_r$ and $\Delta P$ of the BFFP gradually decrease when the flow rate increases. The $Q_r$ and $\Delta P$ are significantly smaller in the negative operation compared with the positive operation. When the BFFP is operating under the design conditions, the $Q_r$ is approximately 3.79 kg/s in the positive direction and approximately 3.06 kg/s in the negative direction. The difference between the $Q_r$ of the two operating conditions is approximately 0.74 kg/s.
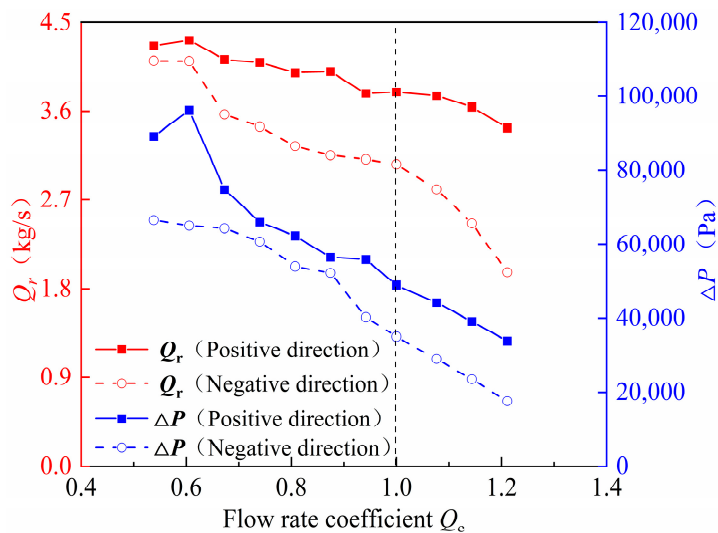


**Figure 9.** The SRC reflux flow and PD at each flow rate.

Since the performance of the pump unit is obviously influenced by the pattern of flow, the reason for the difference in performance between the two operating directions of the pump could be found by analyzing the flow pattern of the impeller inlet. The inlet conditions of the impeller can be judged from the two parts of flow uniformity $V_u$ (FU) and velocity-weighted average angle $\theta$ (VAA). Figure 10 shows the comparison of FU and

VAA for the pump impeller inlet. From the figure, it can be found that in both operating directions, the FU and VAA have the same changing trend. When the flow rate increases, the FU gradually increases, while the VAA first decreases and then increases. In the positive operation, the water enters the impeller at a higher velocity-weighted average angle after passing through the inlet guide vane because the inlet guide vane is the straight vane type. In the negative operation, due to the diffused shape of the rear guide vane, the water passes through the rear guide vane with a pre-swirl and therefore enters the impeller at a lower velocity-weighted average angle than in the positive operation. Similarly, at low flow rates and design conditions, the velocity uniformity at the impeller inlet is slightly better in the positive operation than in the negative operation. In summary, the inlet conditions at the impeller inlet are better in positive operation than in the negative operation for the BFFP, which is one of the reasons why the positive performance of the pump is better than the negative performance.

$$V_u = \left( 1 - \frac{1}{V_a} \sqrt{\frac{\sum\limits_{i=1}^{n} (V_{ai} - V_a)^2}{n}} \right) \times 100\% \tag{7}$$

where $n$ represents the number of grids; $V_{ai}$ represents the axial velocity of the $i$th grid node, m/s; $V_a$ represents the average axial velocity, m/s.

$$\theta = \frac{\sum\limits_{i=1}^{n} \left( 90^\circ - \arctan\frac{V_{ti}}{V_{ai}} \right) V_{ai}}{\sum\limits_{i=1}^{n} V_{ai}} \tag{8}$$

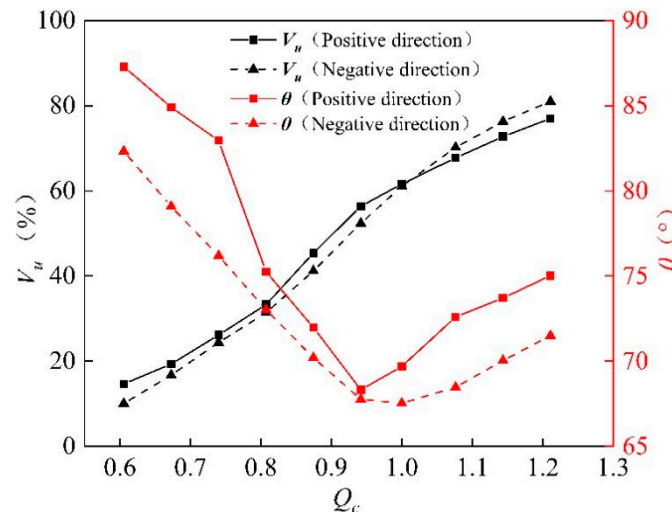where $V_{ti}$ represents the transverse velocity of the $i$th grid node, m/s.



**Figure 10.** FU and VAA of impeller inlet at each flow rate.

The work capacity of the impeller is influenced by factors such as the shape of the blades and the inlet water flow pattern, so the pressure distribution on the surface of the blades of the BFFP can be studied. Figure 11 shows the pressure distribution $P_s$ on the surface of the blade at a span equal to 0.9. Steamwise equal to 0 means at the head of the blade. Steamwise equal to 1 means at the tail of the blade. It can be found that the PD at the head of the blade is much larger than at the tail. As the flow rate increases, the PD between the pressure side (PS) and the suction side (SS) of the blade becomes smaller and smaller. When at a 0.67 $Q_d$ operating condition, the pressure distribution on the PS is larger

in the positive operation than in the negative operation, and the pressure distribution on the suction side is smaller in the positive operation than in the negative operation. In design- and high-flow conditions, the difference in pressure distribution on the PS of the blades is small, and the pressure on the SS of the blades is significantly smaller in the positive than in the negative operation. In the negative operation, the PD between the PS and the SS of the blade is distinctly smaller than that in the positive operation. This is the fundamental reason why the positive performance of the BFFP unit is better than the negative performance.
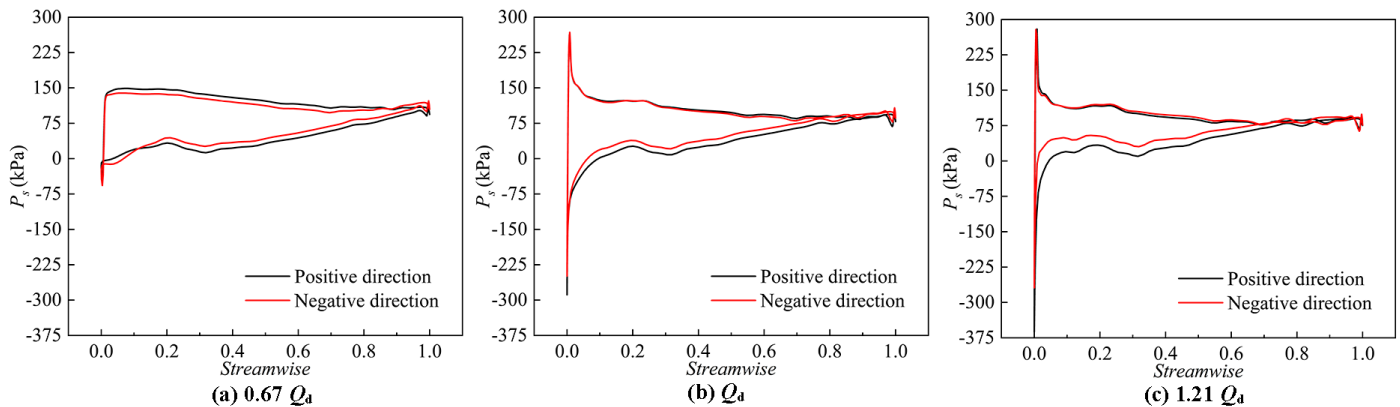


**Figure 11.** Pressure distribution on the blade surface at each flow rate.

The SRC reflux flow is a kind of reflux unique to FFP. When the flow rate is too large, the impeller inlet conditions will be more negatively affected, while a too-small flow rate will not be conducive to motor lubrication and heat dissipation. Therefore, the SRC reflux flow should be controlled in a suitable range. The three-dimensional parameter map within the pump section was extracted and is shown in Figure 12. To research the impact of SRC reflux on the pattern of flow in the pump, the pressure and flow line diagrams of the impeller chamber during the positive and negative operations were taken out, as shown in Figures 13 and 14. To clearly show the position and perspective of the analysis in Figures 13 and 14. From the diagram, it can be found that the flow pattern inside the impeller is relatively smooth. There are two vortexes (red circle area) in the SRC, where the reflux stays and can play a role in reducing the motor temperature and lubrication. When the flow rate decreases, the larger the SRC reflux flow, the greater the effect of the reflux on the impeller inlet flow pattern. Whether a positive or negative operation, at a small flow rate, the reflux impacts the main flow in the impeller inlet side shroud area due to the large SRC reflux flow. Two vortexes appear on both sides of the clearance outlet (impeller inlet) under the action of wall shear force. The vortex on the front side of the clearance outlet is larger, while the vortex on the back side of the clearance outlet is smaller. At the same time, the impeller outlet near the hub also appears a wide range of reflux vortex. When at a $Q_d$ and 1.21 $Q_d$ operating condition, due to the small flow rate of the reflux, the main water flow at the inlet near the shroud only appears a slight offset flow, and no bad flow conditions, such as a vortex, are generated. When at the same flow rate the pressure gradient at the impeller inlet and outlet in the negative direction is smaller than that in the positive direction, which is consistent with the conclusion drawn in Figure 10. When at a 0.67 $Q_d$ operating condition, the range of vortices in positive direction is also greater than in negative direction because the SRC reflux flow is greater in positive direction.
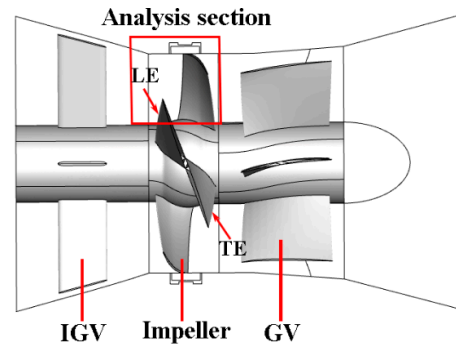
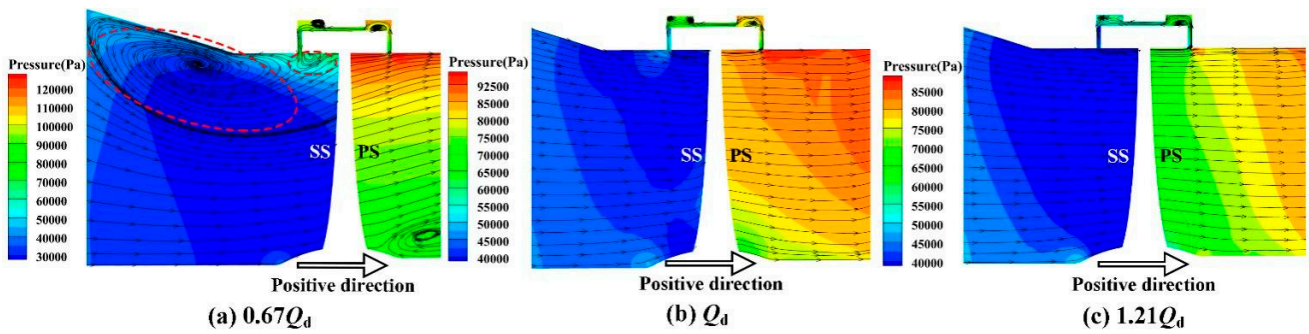**Figure 12.** Schematic diagram of the flow field analysis area.



**Figure 13.** Pressure and flow line distribution of impeller at each flow rate during positive operation.
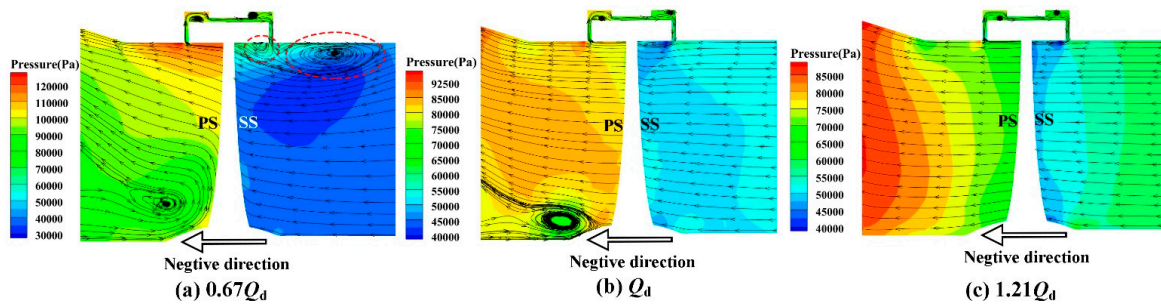


**Figure 14.** Pressure and flow line distribution of impeller at each flow rate during negative operation.

### 3.2. Entropy Production Analysis

Mechanical energy loss occurs all the time during the operation of the water pump, and the process is irreversible, so the increment of EPR in the unit is always greater than 0. The fluid velocity in turbulent motion is divided into two parts, namely, the average velocity and the fluctuating velocity [35–37], so the local EPR $S_E$ of the fluid also includes two parts, and its formula is as follows:

$$S_E = S_{DE} + S_{TE} \tag{9}$$

where $S_{DE}$ is the viscous dissipative EPR, W/m³/K and $S_{TE}$ is the turbulent dissipative EPR, W/m³/K.

$$S_{DE} = \frac{2\mu}{T}\left[\left(\frac{\partial \overline{u}}{\partial x}\right)^2 + \left(\frac{\partial \overline{v}}{\partial x}\right)^2 + \left(\frac{\partial \overline{w}}{\partial x}\right)^2\right] + \frac{\mu}{T}\left[\left(\frac{\partial \overline{u}}{\partial y} + \frac{\partial \overline{v}}{\partial x}\right)^2 + \left(\frac{\partial \overline{u}}{\partial z} + \frac{\partial \overline{w}}{\partial x}\right)^2 + \left(\frac{\partial \overline{v}}{\partial z} + \frac{\partial \overline{w}}{\partial y}\right)^2\right] \tag{10}$$

$$S_{TE} = \frac{\rho \varepsilon}{T} \tag{11}$$

In addition to the above two types of EP, there is also wall EPR $S_{WE}$ in the near-wall region, and its formula is:

$$S_{WE} = \frac{\tau \cdot v}{T} \tag{12}$$

where $T$ is the temperature and is taken as constant room temperature 298.15 K in the calculation; $v$ is the velocity of the first layer mesh node of the wall, m/s; and $\tau$ is the wall shear force, Pa.

The EP can be obtained by volume fractionation of the above three types of EPR, with the total EP $\Delta S_{pro}$ being the sum of the fractions [38], which are given by

$$\Delta S_{pro,DE} = \int_V S_{DE} dV \tag{13}$$

$$\Delta S_{pro,TE} = \int_V S_{TE} dV \tag{14}$$

$$\Delta S_{pro,WE} = \int_A S_{WE} dA \tag{15}$$

$$\Delta S_{pro} = \Delta S_{pro,DE} + \Delta S_{pro,TE} + \Delta S_{pro,WE} \tag{16}$$

where $\Delta S_{pro,DE}$ is the viscous dissipative EP, W/K; $\Delta S_{pro,TE}$ is the turbulent dissipative EP, W/K; $\Delta S_{pro,WE}$ is the wall EP, W/K; $A$ is the wall area of BFFP, m$^2$; and $V$ is the volume of BFFP, m$^3$.

In order to visualize the flow instability region inside the unit and to visualize the energy loss, the EPR inside the pump unit is calculated. Figure 15 shows the EP of each component of the pump unit for three operating conditions. Figure 16 shows the EPR distribution in the pump unit for both directions of operation. The EPR distribution of the SRC, impeller, GV and IGV profiles are selected for demonstration, respectively.
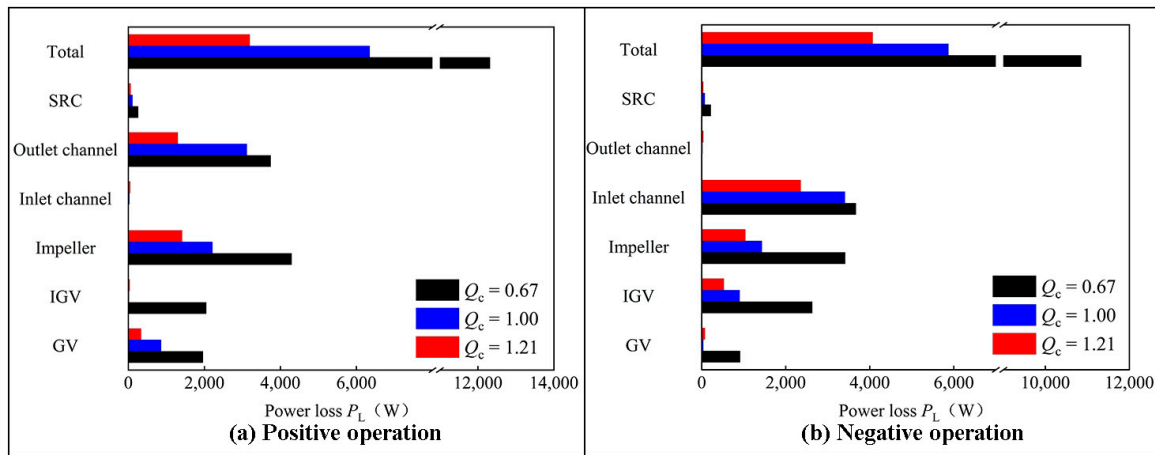


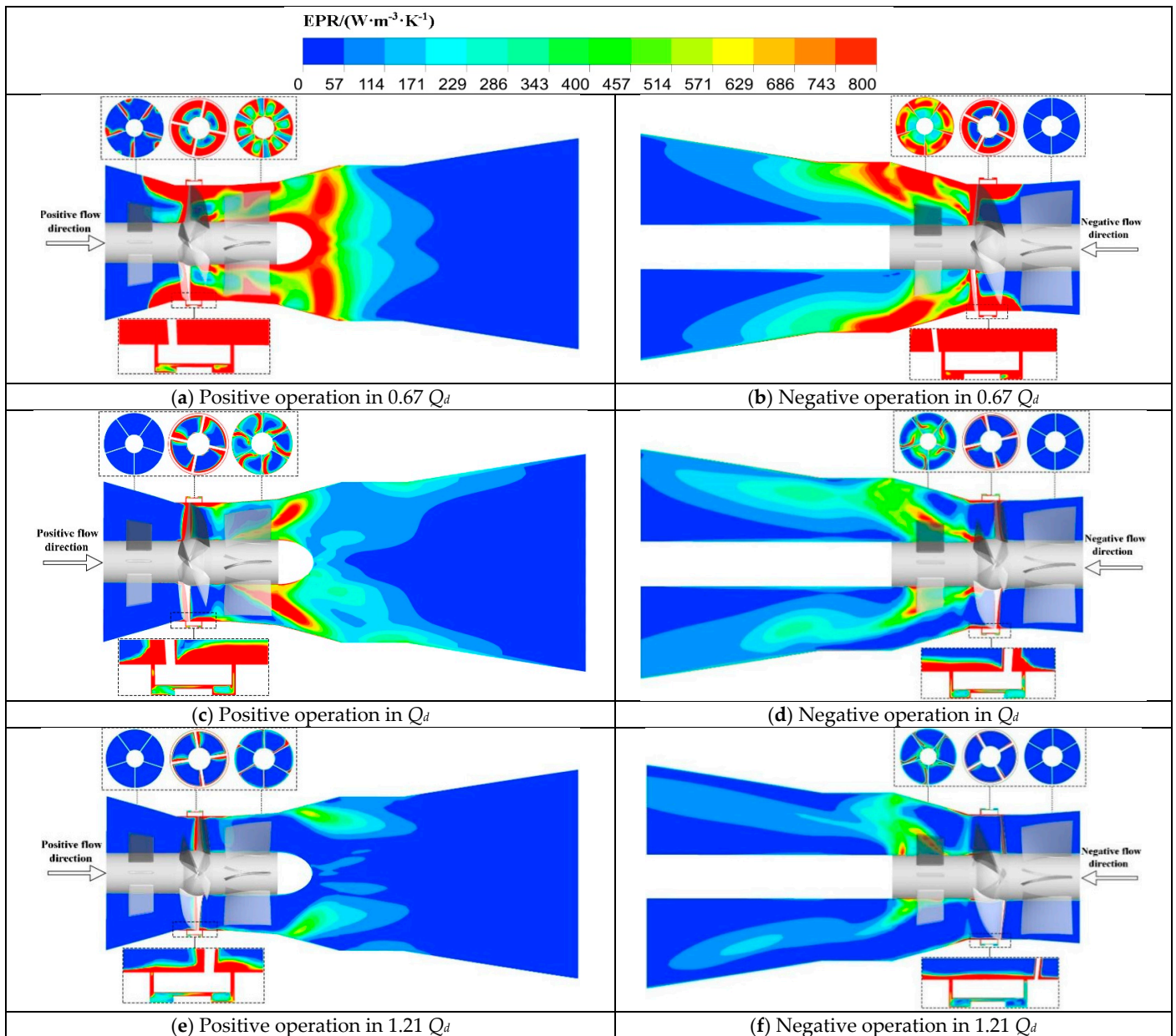**Figure 15.** EP of each part of the pump unit.

**Figure 16.** EPR distribution in the pump unit.

As the flow rate decreases, the EPR inside the BFFP unit gradually increases, and the high EPR range gradually extends to the impeller inlet direction. Since the EPR inside the unit is mainly generated by various bad flow patterns and the collision and friction between water and wall, the EPR is mainly concentrated at the solid wall surface of the impeller chamber and the wall of each overflow component downstream of the impeller. Due to the hedging of the SRC reflux and the mainstream, the impeller inlet flow is more turbulent, and the EPR in the area near the shroud is very high. Especially in small flow rate, the flow rate of the SRC reflux and the high EPR region gradually extends toward the impeller inlet, in which the high EPR area appears in nearly half of the impeller blade radial direction. Under low-flow operation, the reflux flow in the clearance is higher, and the entire clearance is a high EPR region and the range of this high EPR area is larger than the other two flow conditions. Because the reflux flow is small compared with the total flow, the EPR in the SRC is negligible.

The total EPR of the BFFP is about 1.27 times, 1.13 times and 1.08 times higher in the positive operation than in the negative operation at 0.67 $Q_d$, $Q_d$ and 1.21 $Q_d$ flow rates.

In particular, the difference in EPR between two running directions at 0.67 $Q_d$ operating condition is greater, resulting in a significantly lower performance of the pump in negative running than in positive running. When at the $Q_d$ operating condition, the EPR of the impeller in the positive operation accounts for about 35% of the total EPR, while the EPR of the impeller chamber in the negative operation accounts for about 58% of the total EPR, which shows that the energy exchange inside the impeller in the negative operation is more obvious.

### 3.3. Pressure Pulsation Analysis

Before studying the PP of the BFFP, two dimensionless parameters, PP coefficient $C_P$ and PP intensity (PPI) $C_P{}^*$, are introduced to enhance the comparability between the data [39–42]. The PPI is determined in CFD-POST using the standard deviation algorithm, which is defined according to a statistical approach and is a dimensionless parameter. The PPI represents a composite measure of the resultant over one cycle at the network interface, independent of the specific instantaneous rotational position at which the impeller is located. The concept of PPI, therefore, provides a comprehensive and accurate quantitative analysis of the non-stationary flow phenomena in the inlet and outlet sections of the impeller. The equations for PP coefficient and PPI, respectively, are

$$C_P = \frac{P_i - \overline{P}}{0.5\rho u^2} \tag{17}$$

$$C_P{}^* = \sqrt{\frac{\sum\limits_{i=1}^{n} C_P{}^2}{N_t}} \tag{18}$$

where $N_t$ represents the number of steps in one revolution of the impeller, and its value is 180; $\overline{P}$ represents the average pressure, Pa; $\rho$ represents the liquid density, kg/m$^3$; $P_i$ represents the transient pressure, Pa; and $u$ represents the circumferential velocity of the impeller shroud, m/s.

The performance of BFFP differs greatly during the positive and negative operation, so the PP characteristics will also be different. The PPI distribution of two planes of impeller inlet and outlet (as shown in Figure 17) are taken out, as shown in Figures 18–21.
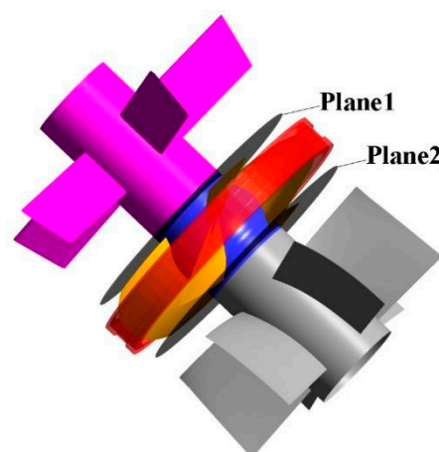


**Figure 17.** Three-dimensional schematic diagram of impeller inlet and outlet profiles.
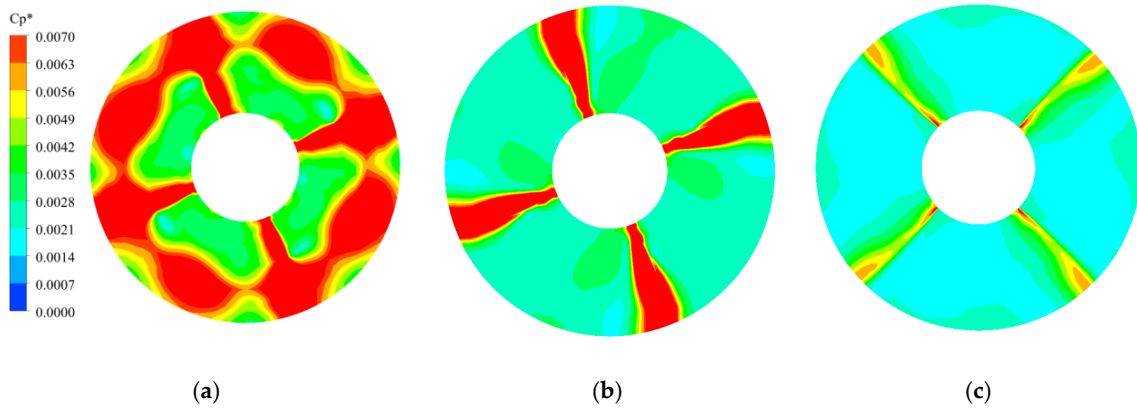
**Figure 18.** PPI distribution at impeller inlet (Plane1) during positive operation. (**a**) 0.67 $Q_{\mathrm{d}}$ (**b**) $Q_{\mathrm{d}}$ (**c**) 1.21 $Q_{\mathrm{d}}$.
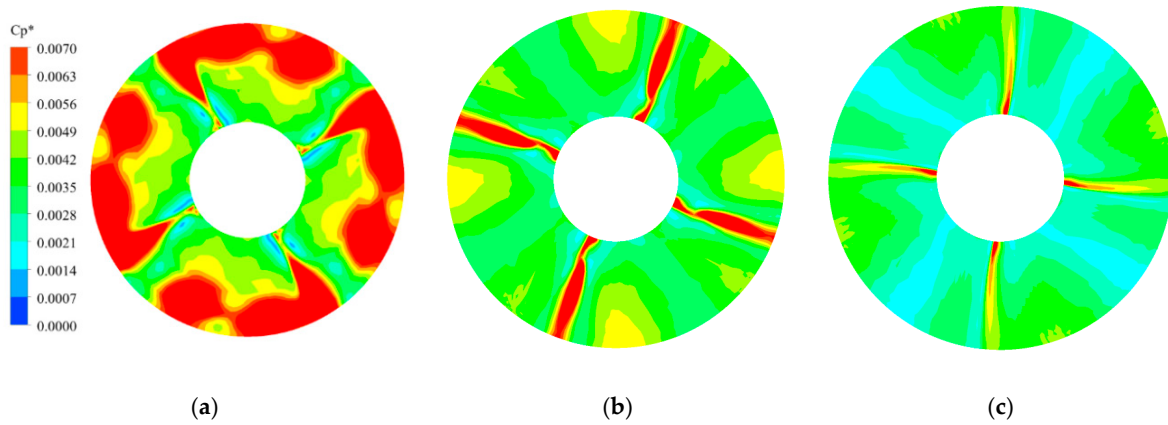


**Figure 19.** PPI distribution at impeller inlet (Plane2) during negative operation. (**a**) 0.67 $Q_{\mathrm{d}}$ (**b**) $Q_{\mathrm{d}}$ (**c**) 1.21 $Q_{\mathrm{d}}$.
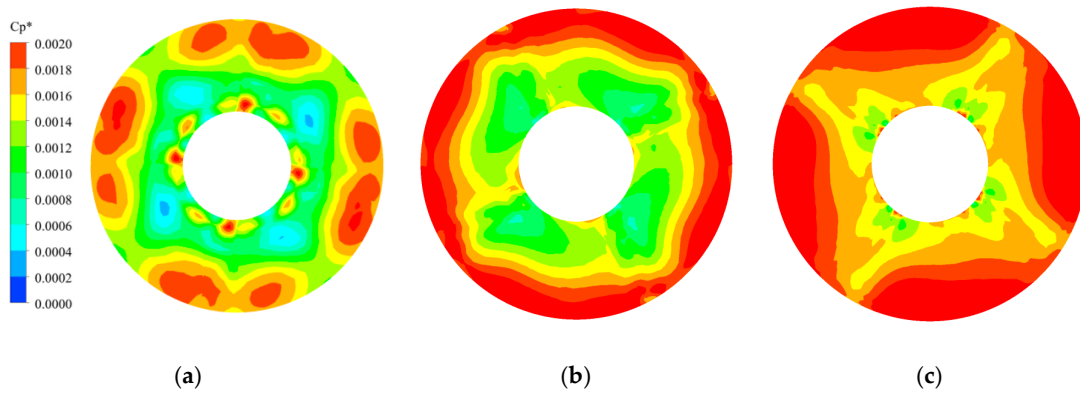


**Figure 20.** PPI distribution at impeller outlet (Plane1) during negative operation. (**a**) 0.67 $Q_{\mathrm{d}}$ (**b**) $Q_{\mathrm{d}}$ (**c**) 1.21 $Q_{\mathrm{d}}$.

**Figure 21.** PPI distribution at impeller outlet (Plane2) during positive operation. (**a**) 0.67 $Q_d$ (**b**) $Q_d$ (**c**) 1.21 $Q_d$.
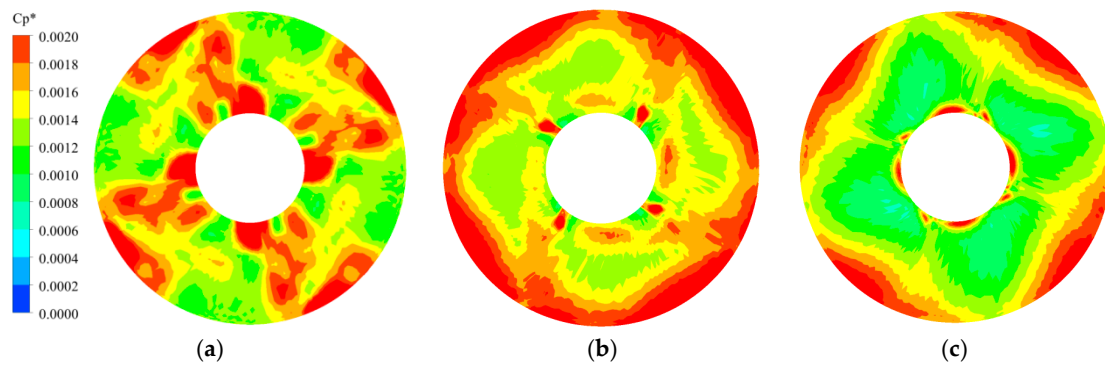
From Figures 18–21, it can be seen that there are four uniformly distributed high pulsation areas in both the inlet and outlet of the impeller, both in the positive and negative operation. This is due to the fact that the internal pulsation of the unit is mainly caused by the periodic collision of the blade with the water flow. Under low flow conditions, the PPI is higher at the impeller inlet near the shroud area due to the large interference of the SRC reflux to the main flow. The area of high PPI is approximately half the impeller diameter. As the flow decreases, the PPI of the impeller inlet gradually increases in both operating directions; the PPI of the impeller outlet gradually increases in the positive operation, while it first increases and then decreases in the negative operation.

The PP of the BFFP is concentrated in two positions of the impeller inlet and outlet for research, where P1 is placed in the middle of the IGV and impeller, and P2 is placed in the middle of the impeller and GV, as shown in Figure 22. Figures 23 and 24 show that the primary frequency of PP at the impeller inlet and outlet is BPF regardless of whether the BFFP is operating in a positive or negative direction. The amplitude of PP at the impeller inlet is greater than that at the impeller outlet. In the design condition, the primary frequency of PP at the impeller inlet in the positive and negative operation is 3.01 and 3.65 times that at the impeller outlet, respectively. The difference of the PP amplitude between impeller inlet and outlet in the negative operation is larger. At a high flow rate, the amplitude of PP at the impeller inlet and outlet during negative operation is smaller than that during the positive operation. In the other two flow rates, in the pump in a negative operation, the impeller inlet and outlet PP amplitude are greater than the positive operation.
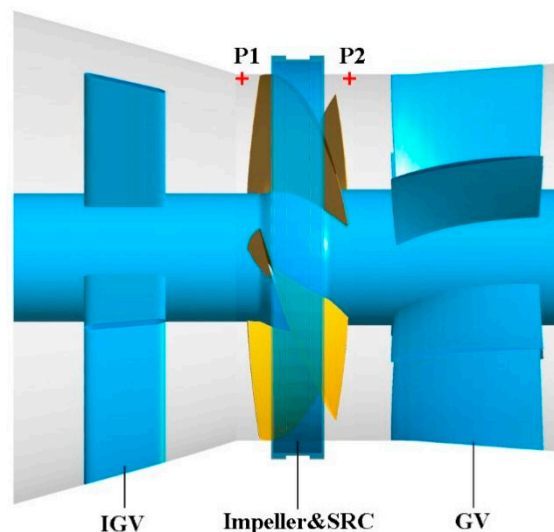


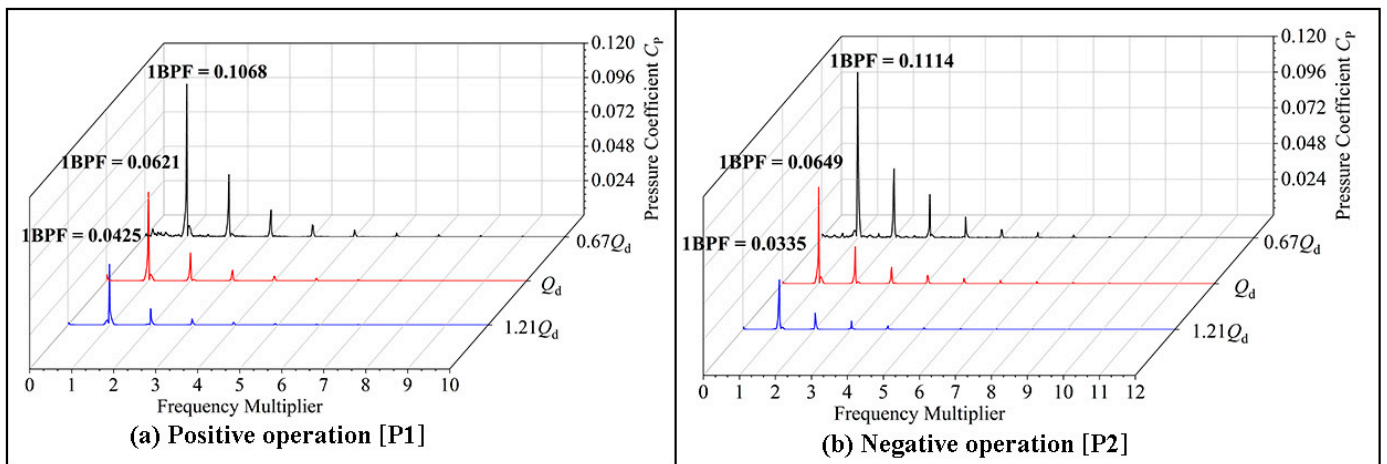**Figure 22.** PP calculation monitoring point.

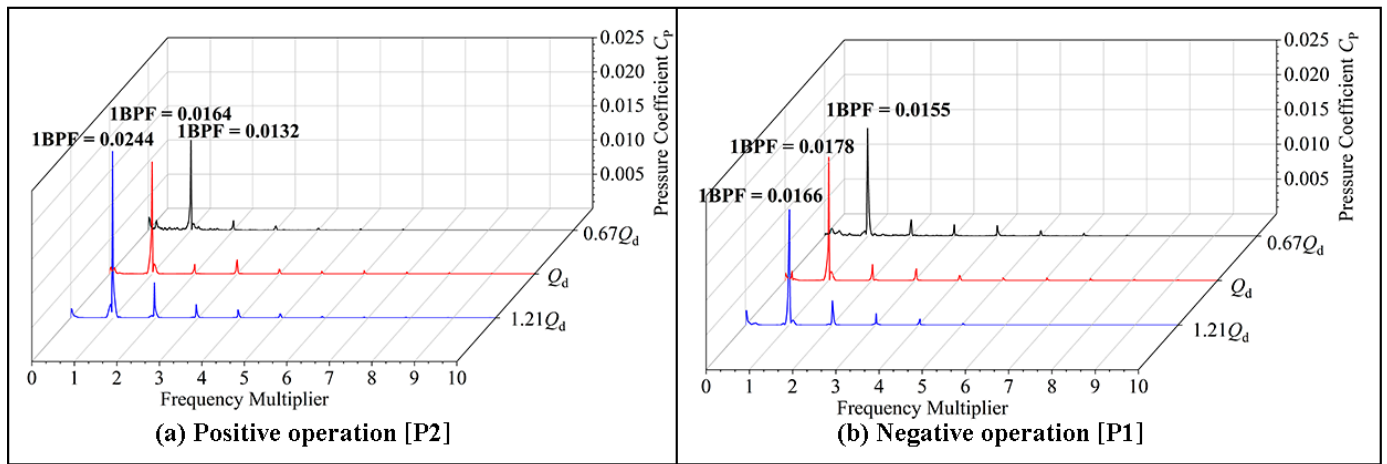**Figure 23.** Frequency domain analysis of PP at impeller inlet.



**Figure 24.** Frequency domain analysis of PP at impeller outlet.

## 4. Verification of Numerical Model Accuracy

### 4.1. Introduction to the Test System

The external characteristics and PP test of the BFFP were carried out on the high-precision hydraulic mechanical test bench of Yangzhou University. The three-dimensional schematic diagram of the hydraulic mechanical test bench is shown in Figure 25. The test bench is a closed circulation system composed of a hydraulic circulation system, power system, control system and measurement system. All parts of the BFFP device were finely processed and assembled. The impeller was machined from brass material and has four blades. The impeller diameter was 300 mm and the hub ratio was 0.4. The rotor was made of plastic steel material and installed on the outer edge of the blade. The blade numbers of IGV and GV were five and six, respectively, among which IGV adopts straight blades and GV adopts diffuse blades. Both IGV and GV blades were 5 mm thick and made of stainless steel. The layout of the BFFP device and PP measuring points is shown in Figure 26. PP sensors M1, M2 and M3 were, respectively, arranged at the IGV water inlet, the impeller water inlet and the impeller outlet. The IGV, impeller and GV are shown in Figure 26a–c, respectively.
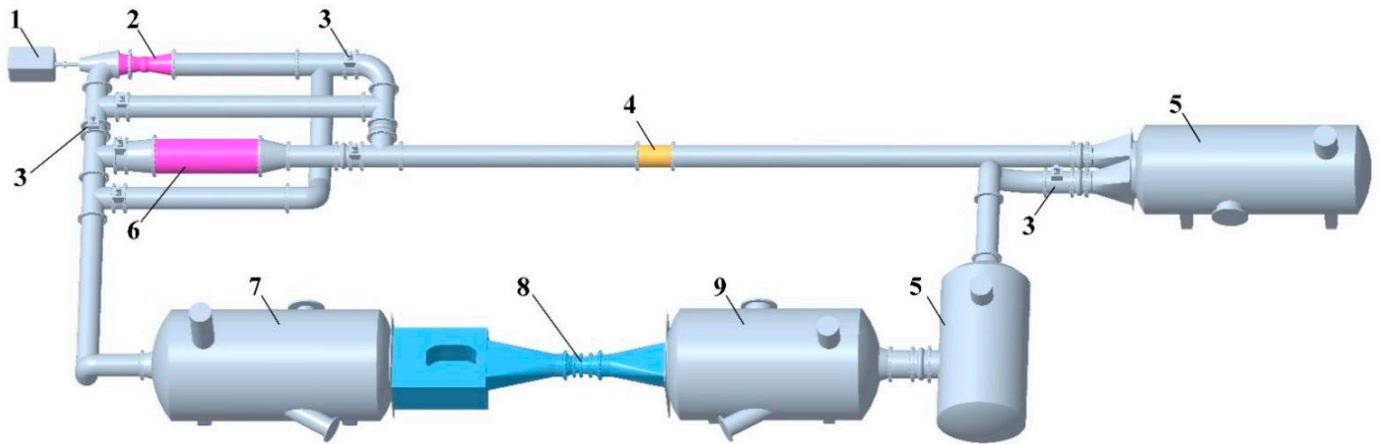
**Figure 25.** Three-dimensional schematic diagram of the BFFP test system (1. Motor; 2. Auxiliary pump No. 1; 3. Electric control valves; 4. Electromagnetic flowmeter; 5. Water storage tanks; 6. Auxiliary pump No. 2; 7. Vacuum water tank; 8. BFFP test section; 9. Pressure water tank).
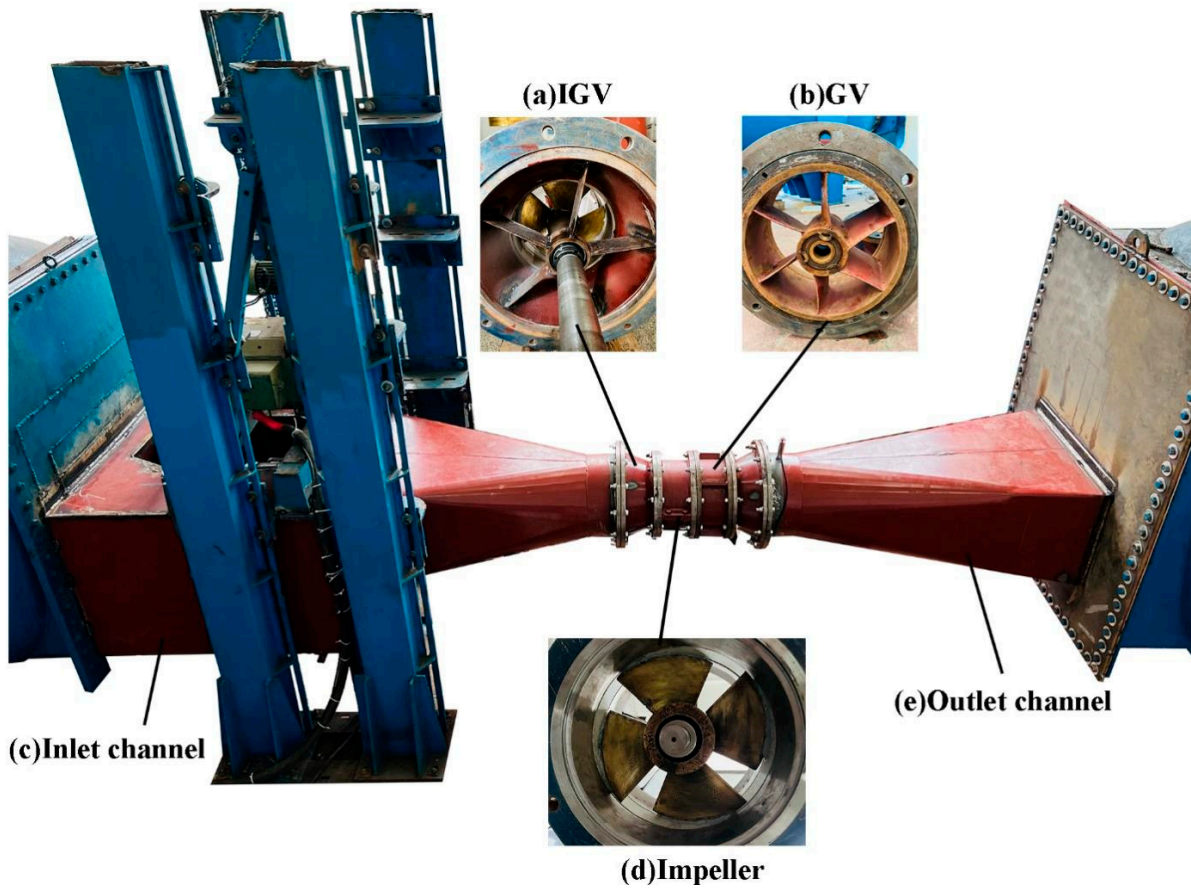


**Figure 26.** Physical diagram of the BFFP unit: (**a**) IGV; (**b**) GV; (**c**) inlet channel; (**d**) impeller; (**e**) outlet channel.

When data acquisition is performed on a BFFP device, there is uncertainty in the measurement results due to imperfect corrections for systematic and random effects. This uncertainty is composed of systematic uncertainty and random uncertainty. The smaller the uncertainty, the higher the accuracy of the measurement result. The combined uncertainty $E_\eta$ is the sum of the squares of the system uncertainty $(E_\eta)_S$ and the random uncertainty $(E_\eta)_r$ with a root.

$$E_\eta = \pm\sqrt{(E_\eta)_S^2 + (E_\eta)_r^2} = \pm 0.2598\%$$

(19)

The combined uncertainty $E_\eta$ of the efficiency test of the pump unit is $\pm0.2598\%$, which is equivalent to the requirements of ISO 9906: 2012 level 1 ($\delta\eta \leq \pm2.9\%$).

### 4.2. External Characteristics

Since a steady-state calculation is required before the transient calculation, the results of the steady-state calculation can also be used to verify the accuracy of the numerical simulation. Figure 27 shows the comparison between the numerical simulation and the model test of the BFFP. Through comparison, it was found that during the positive and negative operation of the pump device, the head curves calculated and tested under high flow rate have a high degree of agreement. As the flow rate decreases, the pump unit enters an unstable operating condition, so the error in the test and calculation increases. The deviation at low flow rates is relatively large, but the maximum deviation does not exceed 3%. This shows that the numerical simulation of BFFP is accurate and reliable.
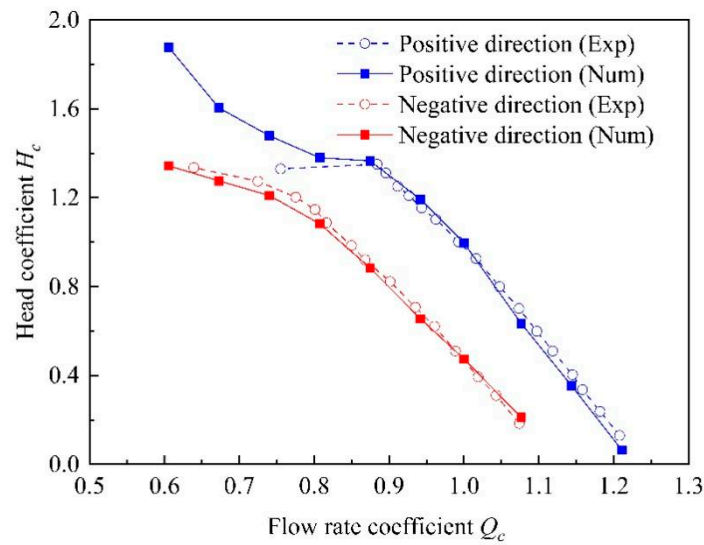


**Figure 27.** Experimental and numerical simulation results of BFFP.

### 4.3. Pressure Pulsation Results

As the PP data collected in the test are transient data, they can be used to verify the accuracy of the transient calculation. The PP experiment tested the PP of the impeller inlet under the design conditions during positive and negative operation, respectively. The sampling time was 20 s, and the sampling interval was 0.001 s. Figure 28 shows the comparison of experimental and computational results. It can be found from the figure that the main frequency of PP at the measuring point at the impeller inlet is 94.73 Hz regardless of positive or negative operation. This frequency is 1 times the blade passing frequency (BPF). The overall difference between the calculated value of PP and the test results is not large, and the positions of the major frequency and the minor frequency are consistent. This shows that the transient simulation results of the BFFP device are accurate.

**Figure 28.** Numerical calculation and test results of PP at impeller inlet under design condition.

### 5. Conclusions

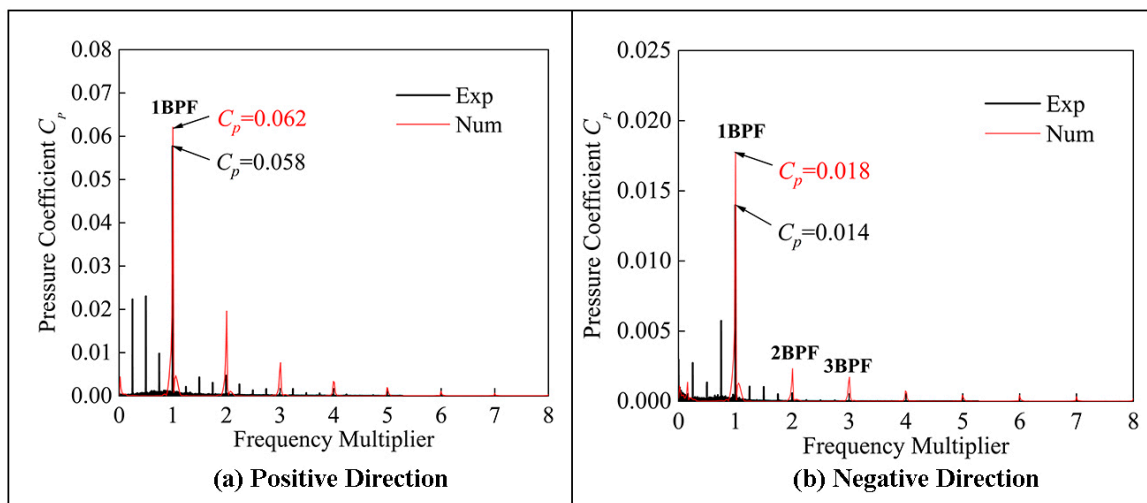In this study, unsteady numerical simulations of a BFFP unit were performed. The performance of the unit was investigated in both positive and negative directions by means of external characteristics, internal flow field, EPR and PP. The pump unit was tested by model tests and compared with calculations to confirm the accuracy of the simulation. The research in this paper leads to the following conclusions.

(1) The performance of BFFP is significantly better in the positive operation than in the negative operation. The difference in head between positive and negative operation is about 1.46 m, the difference in efficiency is about 4.92% and the difference in shaft power is about 4.94 Kw at $Q_d$ operating condition. The PD at the head of the blade is greater than that at the tail. From the blade head to the tail, the PD on the blade surface gradually decreases. When the flow rate decreases, regardless of positive or negative operation, the SRC reflux flow rate increases, the PD between the inlet and outlet of the impeller increases, the FU of the impeller inlet increases gradually, and the VAA decreases first and then increases. During the positive direction of the unit, the clearance reflux flow rate, the FU and the VAA of the impeller inlet are significantly larger than those in the negative operation.

(2) When the BFFP is operating at a low flow rate, the clearance reflux disturbs the main water flow in the impeller inlet near the shroud area, and two vortices appear on both sides of the clearance outlet. During the design-flow and high-flow operation, the flow at the impeller inlet near the shroud edge is deflected to a certain extent due to the small flow rate of the clearance reflux. At low-flow condition, the overall range of inlet vortex is larger than in negative operation due to the larger clearance reflux flow in positive operation of the pump.

(3) Regardless of positive or negative direction, as the flow rate decreases, the EPR inside the BFFP device gradually increases, and the high EPR range gradually extends to the impeller inlet direction. The EPR inside the device is mainly concentrated on the blade surface, the shroud, the hub and the wall of each over-flow component after passing the impeller. At the 0.67 $Q_d$ and $Q_d$ operating condition, the total EPR of the bi-directional unit is greater in positive operation than in negative operation. However, the total EPR of the pump unit in negative operation at 1.21 $Q_d$ is greater than that of the positive operation condition.

(4) The main frequency of PP at the impeller inlet is greater than that at the impeller outlet when the unit operates in both directions, and when the flow rate decreases, the PPI of the impeller inlet increases. At a 0.67 $Q_d$ operating condition, the difference between the main frequency of PP at the impeller inlet and outlet is much larger than other two flow conditions. When at the 0.67 $Q_d$ and $Q_d$ operating condition, the amplitude

of PP in the positive operation is smaller than that in the negative operation. When at the 1.21 $Q_d$ operating condition, the amplitude of PP in the positive operation is larger than that in the negative operation. When the flow rate decreases, the PPI at the impeller outlet increases in the positive operation, while it first increases and then decreases in the negative operation.

(5)  The calculated and experimental data of the BFFP show very little deviation in trend and amplitude. It shows that it is credible to use numerical simulation to study the performance of the BFFP.

**Author Contributions:** H.J.: Data curation, methodology, software, writing. S.C.: Theoretical guidance, financial support. M.W.: Review, editing. H.L.: Experimental guidance. All authors have read and agreed to the published version of the manuscript.

**Institutional Review Board Statement:** Not applicable.

**Informed Consent Statement:** Not applicable.

**Data Availability Statement:** Upon request, all data included in this study can be obtained by contacting the corresponding author.

**Conflicts of Interest:** The authors declare that they have no known competing financial interests or personal relationships that could have appeared to influence the work reported in this paper.

## Abbreviations/Nomenclature

**Abbreviations**

| | |
|---|---|
| BFFP | Bi-directional full-flow pump |
| FFP | Full-flow pump |
| IGV | Inlet guide vane |
| GV | Guide vane |
| SRC | Stator-rotor clearance |
| EP | Entropy production |
| EPR | Entropy production rate |
| BPF | Blade passing frequency |
| PS | Pressure side |
| SS | Suction side |
| PD | Pressure difference |
| PP | Pressure pulsation |
| PPI | Pressure pulsation intensity |
| FU | Flow uniformity |
| VAA | Velocity-weighted average angle |

**Nomenclature**

| | |
|---|---|
| $d_r$ | Hub ratio |
| $dt$ | Single time step |
| $t$ | Total time |
| $D$ | Impeller diameter, mm |
| $D_1$ | Hub diameter, mm |
| $n$ | Impeller revolution, r/min |
| $d$ | The dimension of SRC, mm |
| $\Delta P$ | Pressure difference, Pa |
| $\eta$ | Efficiency, % |
| $Q$ | Flow, kg/s |

| | |
|---|---|
| $Q_d$ | Design flow, L/s |
| $Q_c$ | Flow coefficient, L/s |
| $H$ | Head, m |
| $H_d$ | Design head, m |
| $H_c$ | Head coefficient |
| $C_p$ | Pressure pulsation coefficient |
| $C_p{}^*$ | Pressure pulsation intensity |
| $\overline{P}$ | Average pressure, Pa |
| $P_i$ | Instantaneous pressure, Pa |
| $\rho$ | Liquid density, kg/m$^3$ |
| $u$ | Circumferential velocity, rad/s |
| $N_t$ | Number of steps in one revolution of the impeller |
| $P_s$ | Pressure distribution on the blade surface, kPa |
| $P_L$ | Energy loss |
| $u_i, u_j$ | Time-averaged velocity component |
| $\alpha_k, \alpha_\varepsilon$ | The coefficients of $k$ and $\varepsilon$ |
| $U'$ | Velocity component |
| $\mu_t$ | Turbulent viscosity |
| $x_i, x_j$ | Coordinate component |
| $\overline{B}$ | Sum of additional forces |
| $\mu_{eff}$ | Effective turbulent flow viscosity coefficient |
| $P'$ | Static pressure, Pa |
| $V_u$ | Flow uniformity, % |
| $V_{ai}$ | Axial velocity of the $i$-th grid node, m/s |
| $\theta$ | Velocity weighted average angle, $^\circ$ |
| $V_a$ | Average axial velocity, m/s |
| $\Delta H$ | Average static pressure, Pa |
| $V_{ti}$ | Lateral velocity of the $i$-th grid node, m/s |
| $m$ | Number of grids of the impeller inlet section |
| $T$ | Temperature, $^\circ$C |
| $v$ | is the velocity of the first layer mesh node of the wall, m/s |
| $\tau$ | is the wall shear force, Pa. |
| $S_E$ | local entropy production rate, W/m$^3$/K |
| $S_{DE}$ | viscous dissipative entropy production rate, W/m$^3$/K |
| $S_{TE}$ | turbulent dissipative entropy production rate, W/m$^3$/K |
| $S_{WE}$ | Wall entropy generation production rate, W/m$^3$/K |
| $\Delta S_{pro,DE}$ | viscous dissipative entropy production, W/K |
| $\Delta S_{pro,TE}$ | Turbulent dissipative entropy production, W/K |
| $\Delta S_{pro,WE}$ | Wall entropy production, W/K |
| $\Delta S_{pro}$ | Total entropy production, W/K |
| $A$ | Area, m$^2$ |
| $V$ | Volume, m$^3$ |
| $(E_\eta)_S$ | The systematic uncertainty of the test bench |
| $(E_\eta)_r$ | The random uncertainty of the test bench |
| $E_\eta$ | The combined uncertainty of the test bench |

## References

1. Ma, P.; Wang, J. An analysis on the flow characteristics of bi-directional axial-flow pump under negative operation. *Proc. Inst. Mech. Eng. Part A J. Power Energy* **2017**, *231*, 239–249. [CrossRef]
2. Ma, P.; Wang, J.; Li, H. Numerical Analysis of Pressure Pulsation for a Bidirectional Pump under Positive and Negative Operation. *Adv. Mech. Eng.* **2014**, *6 Pt 8*, 730280. [CrossRef]
3. Ma, P.; Wang, J. Influence of geometrical parameters of straight guide vane on the flow field and hydraulic performance of bidirectional pump. *J. Hydraul. Eng.* **2017**, *48*, 1126–1133. (In Chinese)
4. Meng, F.; Yuan, S.; Li, Y. Fluid–structure coupling analysis of impeller in unstable region for a reversible axial-flow pump unit. *Adv. Mech. Eng.* **2018**, *10*, 1–10. [CrossRef]
5. Meng, F.; Pei, J.; Li, Y.; Yuan, S.; Chen, J. Effect of Guide Vane Position on Hydraulic Performance of Two-direction Tubular Pump Unit. *Trans. Chin. Soc. Agric. Mach.* **2017**, *48*, 135–140. (In Chinese)

6.    Liu, H.; Tang, F.; Yan, S.; Li, D. Experimental and Numerical Studies of Cloud Cavitation Behavior around a Reversible S-Shaped Hydrofoil. *J. Mar. Sci. Eng.* **2022**, *10*, 386. [CrossRef]

7.    Tang, F.; Liu, C.; Wang, G.; Xie, W.; Zhou, J.; Cheng, L. Study on a Reversible Axial-flow Pump Installation with S-shaped Conduit. *Trans. Chin. Soc. Agric. Mach.* **2003**, *6*, 50–53. (In Chinese)

8.    Liu, H.; Lin, P.; Tang, F.; Chen, Y.; Zhang, W.; Yan, S. Experimental Study on the Relationship Between Cavitation and Lift Fluctuations of S-Shaped Hydrofoil. *Front. Energy Res.* **2021**, *9*, 813355. [CrossRef]

9.    Ma, P.; Wang, J.; Wang, H. Investigation of performances and flow characteristics of two bi-directional pumps with different airfoil blades. *Sci. China Technol. Sci.* **2018**, *61*, 1588–1599. [CrossRef]

10.   Shi, L.; Zhu, J.; Wang, L.; Chu, S.; Tang, F.; Jin, Y. Comparative Analysis of Strength and Modal Characteristics of a Full Tubular Pump and an Axial Flow Pump Impellers Based on Fluid-Structure Interaction. *Energies* **2021**, *14*, 6395. [CrossRef]

11.   Shi, L.; Jiang, Y.; Cai, Y.; Chen, B.; Tang, F.; Xu, T.; Zhu, J.; Chai, Y. Influence of Inlet Groove on Flow Characteristics in Stall Condition of Full-Tubular Pump. *Front. Energy Res.* **2022**, *10*, 949639. [CrossRef]

12.   Shi, L.; Zhu, J.; Yuan, Y.; Tang, F.; Huang, P.; Zhang, W.; Liu, H.; Zhang, X. Numerical Simulation and Experiment of the Effects of Blade Angle Deviation on the Hydraulic Characteristics and Pressure Pulsation of an Axial-Flow Pump. *Shock Vib.* **2021**, *2021*, 6673002. [CrossRef]

13.   Song, X.; Liu, C.; Wang, Z. Prediction on the pressure pulsation induced by the free surface vortex based on experimental investigation and Biot-Savart Law. *Ocean Eng.* **2022**, *250*, 110934. [CrossRef]

14.   Jiao, H.; Sun, C.; Chen, S. Analysis of the Influence of Inlet Guide Vanes on the Performance of Shaft Tubular Pumps. *Shock Vib.* **2021**, *2021*, 5177313. [CrossRef]

15.   Yang, F.; Li, Z.; Yuan, Y.; Lin, Z.; Zhou, G.; Ji, Q. Study on vortex flow and pressure fluctuation in dustpan-shaped conduit of a low head axial-flow pump as turbine. *Renew. Energy* **2022**, *196*, 856–869. [CrossRef]

16.   Zheng, L.; Chen, X.; Zhang, W.; Zhu, Z.; Qu, J.; Wang, M.; Ma, X.; Cheng, X. Investigation on characteristics of pressure fluctuation in a centrifugal pump with clearance flow. *J. Mech. Sci. Technol.* **2020**, *34*, 3657–3666. [CrossRef]

17.   Gohil Pankaj, P.; Saini, R.P. Investigation into cavitation damage potentiality using pressure pulsation phenomena in a low head Francis turbine for small hydropower schemes. *Ocean Eng.* **2022**, *263*, 112230. [CrossRef]

18.   Al-Obaidi, A.R.; Mohammed, A.A. Numerical Investigations of Transient Flow Characteristic in Axial Flow Pump and Pressure Fluctuation Analysis Based on the CFD Technique. *J. Eng. Sci. Technol. Rev.* **2019**, *12*, 70–79. [CrossRef]

19.   Yang, F.; Chang, P.; Cai, Y.; Lin, Z.; Tang, F.; Lv, Y. Analysis of Energy Loss Characteristics of Vertical Axial Flow Pump Based on Entropy Production Method under Partial Conditions. *Entropy* **2022**, *24*, 1200. [CrossRef]

20.   Yang, F.; Li, Z.; Cai, Y.; Jiang, D.; Tang, F.; Sun, S. Numerical Study for Flow Loss Characteristic of an Axial-Flow Pump as Turbine via Entropy Production Analysis. *Processes* **2022**, *10*, 1695. [CrossRef]

21.   Meng, F.; Li, Y. Energy Characteristics of a Bidirectional Axial-Flow Pump with Two Impeller Airfoils Based on Entropy Production Analysis. *Entropy* **2022**, *24*, 962. [CrossRef] [PubMed]

22.   Feng, J.; Zhang, Y.; Zhu, G.; Li, Y.; Li, W.; Luo, X. Transition process characteristics of centrifugal pump with power-off based on entropy production theory. *Trans. Chin. Soc. Agric. Eng.* **2020**, *36*, 10–17. (In Chinese)

23.   Xie, R.; Tang, F.; Liu, C.; Yang, F.; Shi, L.; Xie, C. Comparison of hydraulic performance between vertical shaft and shaft extension tubular pumping system. *J. Agric. Mach.* **2016**, *32*, 24–30.

24.   Yang, F.; Liu, C.; Zhang, L. Pressure Pulsations of the Blade Region in S-Shaped Shaft-Extension Tubular Pumping System. *Math. Probl. Eng.* **2014**, *2014*, 820135. [CrossRef]

25.   Lijian, S.; Xinquan, L.; Fangping, T.; Yueling, Y.; Rongsheng, X.; Wenpeng, Z. Design Optimization and Experimental Analysis of Bidirectional Shaft Tubular Pump Unit. *J. Agric. Mach.* **2016**, *47*, 85–91.

26.   Liu, J.; Zheng, Y.; Zhou, D.; Mao, Y.; Zhang, L. Analysis of Basic Flow Pattern in Shaft Front-positioned and Shaft Rear-positioned Tubular Pump Systems. *J. Agric. Mach.* **2010**, *41*, 32–38.

27.   Shi, L.; Yuan, Y.; Jiao, H.; Tang, F.; Cheng, L.; Yang, F.; Jin, Y.; Zhu, J. Numerical investigation and experiment on pressure pulsation characteristics in a full tubular pump. *Renew. Energy* **2021**, *163*, 987–1000. [CrossRef]

28.   Shi, L.; Zhang, W.; Jiao, H.; Tang, F.; Wang, L.; Sun, D.; Shi, W. Numerical simulation and experimental study on the comparison of the hydraulic characteristics of an axial-flow pump and a full tubular pump. *Renew. Energy* **2020**, *153*, 1455–1464. [CrossRef]

29.   Yang, F.; Hu, W.; Li, C.; Liu, C.; Jin, Y. Computational study on the performance improvement of axial-flow pump by inlet guide vanes at part loads. *J. Mech. Sci. Technol.* **2020**, *34*, 4905–4915. [CrossRef]

30.   Yang, F.; Liu, C.; Tang, F.; Zhou, J.; Luo, C. Numerical Simulation on Hydraulic Performance of Axial-flow Pumping System with Adjustable Inlet Guide Vanes. *Trans. Chin. Soc. Agric. Mach.* **2014**, *45*, 51–58.

31.   Xie, R.; Wu, Z.; He, Y.; Tang, F.; Xie, C.; Tu, L. Optimization Research on Passage of Bidirectional Shaft Tubular Pump. *Trans. Chin. Soc. Agric. Mach.* **2015**, *46*, 68–74.

32.   Zhang, X.; Tang, F. Investigation on hydrodynamic characteristics of coastal axial flow pump system model under full working condition of forward rotation based on experiment and CFD method. *Ocean Eng.* **2022**, *253*, 111286. [CrossRef]

33.   Mu, T.; Zhang, R.; Xu, H.; Zheng, Y.; Fei, Z.; Li, J. Study on improvement of hydraulic performance and internal flow pattern of the axial flow pump by groove flow control technology. *Renew. Energy* **2020**, *160*, 756–769. [CrossRef]

34.   Jin, Y.; He, X.; Zhang, Y.; Zhou, S.; Chen, H.; Liu, C. Numerical and Experimental Investigation of External Characteristics and Pressure Fluctuation of a Submersible Tubular Pumping System. *Processes* **2019**, *7*, 949. [CrossRef]

35. Kock, F.; Herwig, H. Entropy production calculation for turbulent shear flows and their implementation in CFD codes. *Int. J. Heat Fluid Flow* **2005**, *26*, 672–680. [CrossRef]
36. Kock, F.; Herwig, H. Local entropy production in turbulence shear flows: A high-Reynolds number model with wall functions. *Int. J. Heat Mass Transf.* **2004**, *47*, 2205–2215. [CrossRef]
37. Herwig, H.; Kock, F. Direct and indirect methods of calculating entropy generation rates in turbulent convective heat transfer problems. *Heat Mass Transfer.* **2007**, *43*, 207–215. [CrossRef]
38. Bohle, M.; Fleder, A.; Mohr, M. Study of the losses in fluid machinery with the help of entropy. In Proceedings of the International Symposium on Transport Phenomena and Dynamics of Rotating Machinery, Honolulu, HI, USA, 10–15 April 2016.
39. Meng, F.; Qin, Z.; Li, Y.; Chen, J. Investigation of Transient Characteristics of a Vertical Axial-Flow Pump with Non-Uniform Suction Flow. *Machines* **2022**, *10*, 855. [CrossRef]
40. Wang, J.; Chen, J.; Yuan, S.; Pei, J.; Meng, F. Pressure fluctuation near double volute tongue for double-suction centrifugal pump. *J. Drain. Irrig. Mach. Eng.* **2016**, *34*, 283–289.
41. Wang, W.; Yuan, S.; Pei, J.; Zhang, J.; Yuan, J. Numerical Analysis of the Clocking Effect on the Pressure Fluctuation in the Centrifugal Pump with Vaned Diffuser. *J. Mech. Eng.* **2015**, *51*, 185–192. [CrossRef]
42. Pei, J.; Yuan, S.; Yuan, J.; Wang, W.J. Comparative study of pressure fluctuation intensity for a singleblade pump under multiple operating conditions. *J. Huazhong Univ. Sci. Technol. Nat. Sci. Ed.* **2013**, *41*, 29–33+53.